Wind-driven flow over topography

by Michael A. Spall[1,2]

ABSTRACT

The space and time scales over which wind forcing can directly drive flows over regions of closed topographic contours are explored using an idealized numerical model and theory. It is shown that stratification limits the vertical scale of the mean flow but also results in an enhanced recirculation strength in shallow water by distorting the isopycnals in the bottom boundary layer. Time-dependent forcing can drive flows that extend deeper than the mean flow because the initial response is primarily barotropic. This response is limited at low frequencies by baroclinic Rossby wave propagation. It is expected that these wind-driven flows might be important in the vicinity of islands and over large-scale topographic features.

Keywords: topography, stratified flows, Ekman pumping

1. Introduction

The foundational theory for the wind-driven flow by Sverdrup (1947) did not consider topography. Welander (1968) extended the Sverdrup theory to include topography and found that regions of closed f/h (linear, barotropic potential vorticity) contours subject to weak forcing and weak dissipation could support strong horizontal recirculations, particularly for unstratified cases. This is essentially a result of conservation of potential vorticity, thus rendering closed potential vorticity contours as free advective pathways. Similar strong recirculations within regions of homogeneous potential vorticity arise in the theory of Young and Rhines (1982), where in this case the closed contours are a result of wind-driven deformation of the density interfaces rather than from deviations in bottom topography. de Szoeke (1985) used some ideas from Young and Rhines (1982) to modify the Sverdrup relation to include large-scale topography and stratification, also finding that regions of closed contours of f/h could support strong recirculations. For linear stratified flows, these recirculations are only found if the flow penetrates deep enough to directly feel the bottom topography. Dewar (1998) developed a theory for the eddy-driven circulation over deep topography that can result even if the directly wind-driven flow is trapped in the main

---

1. Woods Hole Oceanographic Institution, MS#21, 360 Woods Hole Road, Woods Hole, MA 02543.
2. Corresponding author: *e-mail: mspall@whoi.edu*

---

thermocline. The previously discussed theories address the mean circulation forced by wind stress curl in either unstratified models or in models with very few vertical layers.

One may also think of these recirculations as being required to close the mass balance. If there is a net wind-driven Ekman transport into a closed contour, this mass must exit somewhere below the surface Ekman layer. For linear flows, in which Reynolds stresses can be neglected in the interior, the most likely means to export this mass is in a bottom Ekman layer. The recirculation along f/h contours is required to drive this bottom boundary layer. This balance was used by Kamenkovich (1962) to develop a model of the Antarctic Circumpolar Current, where it was demonstrated that the current transport was inversely proportional to the bottom friction coefficient. A similar constraint was applied to the regions of closed f/h contours in the Arctic Ocean and Nordic Seas (Nøst and Isachsen 2003). Time-dependent, equivalent barotropic versions of this theory were applied to the Nordic Seas (Isachsen et al 2003) and the Caspian Sea (Ghaffari, Isachsen, and LaCasce 2013) and gave favorable comparisons with the observed ocean currents.

The present study revisits these ideas of wind-driven flows over closed f/h contours. Although the results are broadly relevant to stratified, time-dependent flows, the primary motivation is the strong wind stress curl that is often found in the vicinity of islands. This curl arises as the atmospheric winds navigate around the orography of the island. Some region of closed f/h contours will be found near the island, and, as the topography gets shallow, it is expected that even strong stratification will not be able to shield the flow from the bottom. The net Ekman pumping within any closed topographic contour will also, in general, be nonzero and time dependent, so it is also expected that strong recirculations will result. These results are also relevant for submerged banks, such as Georges Bank, Browns Bank, the Zapiola Rise, and the Kerguelen Plateau, that may be subject to mean or time-dependent wind stress curl. The primary goal of this study is to identify the space and time scales for which such wind stress can force ocean circulations. The basic ideas are developed and tested with a configuration utilizing very idealized forcing and topography.

2. Mean transport

The theoretical development makes use of simple forms of forcing, topography, and stratification in order to allow for closed form solutions and to most clearly expose the dominant scaling that controls the magnitude and spatial and temporal variability of the currents. The wind stress used throughout most of the article is uniform in space, although it can vary in time. Because the problems are configured on a beta plane, this uniform wind stress provides a nearly uniform Ekman pumping velocity, which gives rise to the basic constraint of closing the mass balance within regions of closed f/h contours. Such large-scale forcing may also be relevant for deep, large-scale topographic rises found in the open ocean, such as the Zapiola Rise in the South Atlantic. However, the main results found here relate to the dominant depth and time scales, which will remain relevant for all situations

in which there is a net Ekman pumping into regions of closed f/h contours, whether it be driven by variations in the Coriolis parameter or variations in the wind stress.

Consider a uniformly stratified fluid subject to a spatially uniform wind toward the west. There will be a poleward Ekman transport given by

$$V_E = -\frac{\tau}{\rho_0 f},$$ (1)

where $\tau < 0$ is the surface wind stress, $f = f_0 + \beta y$ is the Coriolis parameter, $y = 0$ at the central latitude of the bottom topography, and ρ_0 is a reference density. Because the Coriolis parameter increases with increasing latitude, the northward Ekman transport decreases, and there is a downwelling of strength:

$$w = \frac{\tau \beta}{\rho_0 f_0^2 (1 + \beta y/f_0)^2} \approx \frac{\tau \beta}{\rho_0 f_0^2}.$$ (2)

Using the previous approximation, which is good for $\beta y/f_0 \ll 1$, the net downwelling within any radius r is then

$$W = \int_0^{2\pi} \frac{\tau \beta r}{\rho_0 f_0^2} \, d\theta = \frac{\pi r^2 \tau \beta}{\rho_0 f_0^2}.$$ (3)

The starting point is the linear, barotropic shallow-water equations on a beta plane, although some baroclinic effects will be considered subsequently.

$$\frac{\partial \vec{u}}{\partial t} + \vec{k} \times \vec{u} f_0 (1 + \beta y/f_0) + C_d \vec{u}/H = -\nabla p/\rho_0 + \frac{\vec{\tau}}{\rho_0 H}$$ (4)

The hydrostatic pressure is given by p, and C_d is a linear bottom drag coefficient. An estimate for the strength of the recirculation along the topographic contours can be derived using a circulation integral of the momentum equations around a closed contour C. A detailed derivation can be found, for example, in Nøst and Isachsen (2003).

$$\frac{\partial}{\partial t} \int_C \vec{u} \cdot d\mathbf{l} + \int_C C_d \vec{u}/H \cdot d\mathbf{l} = \int_C \frac{\vec{\tau}(t)}{\rho_0 H} \cdot d\mathbf{l}$$ (5)

The along-contour direction is $\mathbf{l}$. The integral of the Coriolis term around contour C has been neglected. This is a good approximation if the geostrophic flow is dominated by a recirculation along contour C. So, in the steady state, the downward mass flux forced by the meridional Ekman transport (right-hand side term) is balanced through an export of mass in the bottom boundary layer (second term on the left-hand side). Similar constraints have been used by Young and Rhines (1982), Dewar (1998), Nøst and Isachsen (2003), and Isachsen et al (2003).

The average along-topography velocity U is defined as

$$U = \frac{1}{2\pi r} \int_C \vec{u} \cdot d\mathbf{l}.$$ (6)

If the closed contour C is chosen to follow an f/H contour, then, on that contour, $H = H_0(1+\beta y/f_0)$. Making use of the approximation $1/H \approx (1-\beta y/f_0)/H_0$ on the right-hand side of equation (5), which is valid for $\beta y/f_0 \ll 1$, the solution for U subject to steady wind forcing of $\tau = \tau_0$ is

$$U_b = \frac{\tau_0 \beta r}{2\rho_0 f_0 C_d}, \qquad (7)$$

where the subscript b indicates that this is the bottom velocity. It has also been assumed that the radius of contour C is constant. This is a good assumption when the potential vorticity gradient provided by the topography greatly exceeds the planetary vorticity gradient such that their ratio, $\gamma = \alpha f_0/\beta H$, where α is the bottom slope, is much greater than 1. For typical parameters, $\alpha = 10^{-3}$, $f_0 = 10^{-4}$ s^{-1}, $\beta = 2 \times 10^{-11}$ m^{-1} s^{-1}, $H = 200$ m, and $\gamma = 25$. This simplification results in the potential vorticity contours being coincident with topographic contours and, to leading order, a mean geostrophic flow that is along topographic contours. This solution could also be derived by balancing the export of mass in the bottom Ekman layer, which is $2\pi r C_d U_b/f_0$ with the downward Ekman pumping from the wind stress given by equation (3). The velocity is linearly proportional to the wind stress, is inversely proportional to the bottom drag, and increases linearly with radius.

For simplicity, a conical topography is used that extends from the surface at $y = 0$ and slopes uniformly to a depth of H at radius r with slope $\alpha = H/r$. The depth-integrated barotropic transport streamfunction (subscript BT) can then be calculated as

$$\Psi_{BT} = \int_0^r U_b H \, dr = \frac{\tau_0 \alpha \beta r^3}{6\rho_0 f_0 C_d} = \frac{f_0 H}{6\pi C_d} W. \qquad (8)$$

The strength of the recirculation is given by the Ekman pumping transport within the region of closed f/H contours, W, with a scale factor proportional to the ratio of the damping timescale H/C_d to the inertial timescale f_0^{-1}.

a. Numerical example

The magnitude, horizontal and vertical extent, and vertical structure of the velocity field forced by net downward Ekman pumping are the primary quantities of interest. The previous derivation required the assumption that the flow is linear and that stratification is not important. The transport predicted by equation (8) will be compared with that produced by the Massachusetts Institute of Technology general circulation model (Marshall et al 1997) for both stratified and unstratified configurations on a beta plane, thus allowing for evaluation of these assumptions. The model solves the hydrostatic, primitive equations of motion on a staggered Cartesian C-grid with a partial cell treatment of the bottom topography. Most model calculations are configured in a closed domain of 2,000 km zonal extent and 2,000 km meridional extent. The bottom topography is a cone with slope $\alpha = 10^{-3}$ and maximum depth of 500 m at a radius of 500 km. The model is configured on a beta

plane with $f_0 = 10^{-4}$ s^{-1} and $\beta = 2 \times 10^{-11}$m^{-1} s^{-1}. The linear bottom drag coefficient $C_d = 2 \times 10^{-4}$ m s^{-1}. The horizontal grid spacing is 5 km for most of the calculations and uses 30 levels in the vertical, 10 m thick over the upper 100 m, and 20 m thick over the deepest 400 m. The time-dependent calculations were carried out at 10 km resolution; comparison between a few calculations at 5 km and 10 km grid spacing confirms that the lower resolution is sufficient to capture the basic response.

The Gent McWilliams (GM) (Gent and McWilliams 1990) parameterization for tracer transport is included with a diffusion coefficient of 10 m^2 s^{-1}. Although the model resolves the first baroclinic deformation radius very well, it will be shown subsequently that the downslope flow leads to a steepening of the isopycnals in the bottom boundary layer, which is $O(20)$ m thick. This would likely give rise to very small-scale baroclinic instabilities that would oppose this steepening. The model grid of 5 km is not sufficient to represent these instabilities, and so they are parameterized here. The GM parameterization has not been tested for bottom boundary layers over a sloping bottom, and it is likely that it is missing important aspects, such as the influence of bottom slope on instability. Thus, the use of GM, both in the numerical model and the accompanying theory, should be viewed only as a qualitative demonstration of the influence of the bottom boundary layer on the large-scale circulation.

The model is initialized at rest with either no stratification or a uniform stratification of $N^2 = 2.5 \times 10^{-5}$ s^{-2} (internal deformation radius $NH/f_0 = 25$ km) and an initial surface temperature of 10°C. The stratification is restored toward this uniform initial stratification within 100 km of the model outer boundary in order to suppress influences of the lateral boundaries in the model. Most calculations with steady forcing have been carried out for 10 years simulation, although a few required integrations out to 20 years to arrive at steady state. The model is forced with a uniform zonal wind stress of $\tau_0 = -0.1$ N m^{-2}. The wind stress, stratification, β, f_0, GM diffusion coefficient, bottom slope, and forcing frequency will all be varied from the central values used here (see Table 1).

The mean transport streamfunction for the final year of integration for the central case with stratification is shown in Figure 1 (run 1 in Table 1). The flow is dominated by an anticyclonic recirculation around the topography. The maximum transport is 1.02 Sv, with typical horizontal velocities of several centimeters per second. Because of the southward Sverdrup flow in the basin interior, the recirculation is shifted slightly toward the east relative to the topography. There are also boundary layers along the northern, southern, and western boundaries of the domain, away from the topography, that will not be considered here. The damping regions within 100 km of the boundaries introduce density gradients that are baroclinically unstable, as indicated by the eddies along the western boundary region. Topographic contours are indicated by the white lines, and the red contour is the radial extent expected for the recirculation based on the scaling given subsequently. The strength, extent, and time dependence of this anticyclonic recirculation is the focus of this study.

The azimuthally averaged horizontal velocities and temperature are shown in Figure 2. The radial velocity is dominated by flow toward shallow water in the surface layer and flow toward the deep water near the bottom, at least out to a radius of approximately 250 km. At

Table 1. Parameters for the steady model calculations and symbols used in Figure 5.

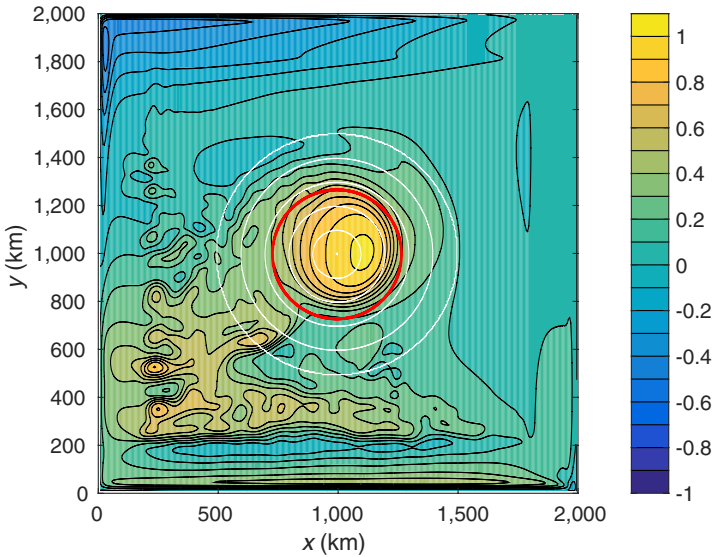| Run	τ_0 (N m^{-2})	f_0 (10^{-4} s^{-1})	β (10^{-11} m^{-1} s^{-1})	N^2 (10^{-5} s^{-2})	κ (m^2 s^{-1})	α	Symbol
1	−0.1	1	2	2.5	10	0.001	Asterisk
2	−0.1	1	1	2.5	10	0.001	Circle
3	−0.1	1	3	2.5	10	0.001	Circle
4	−0.1	1	2	0	10	0.001	Circle
5	−0.1	1	1	0	10	0.001	Circle
6	−0.1	1	0.5	0	10	0.001	Circle
7	−0.1	1	2	1	10	0.001	Triangle
8	−0.1	1	2	0.5	10	0.001	Triangle
9	−0.1	1	2	4	10	0.001	Triangle
10	−0.05	1	2	2.5	10	0.001	Diamond
11	−0.15	1	2	2.5	10	0.001	Diamond
12	−0.1	0.75	2	2.5	10	0.001	Cross
13	−0.1	1.25	2	2.5	10	0.001	Cross
14	−0.1	1	2	2.5	5	0.001	Square
15	−0.1	1	2	2.5	20	0.001	Square
16	−0.1	1	2	2.5	40	0.001	Square
17	−0.1	1	2	2.5	10	0.0025	Star
18	−0.1	1	2	2.5	10	0.005	Star

Figure 1. Mean depth-integrated transport streamfunction over the final year of integration. White lines mark the topographic contours; the red line is the scaling estimate of the maximum radius of recirculation R_m given by equation (10).
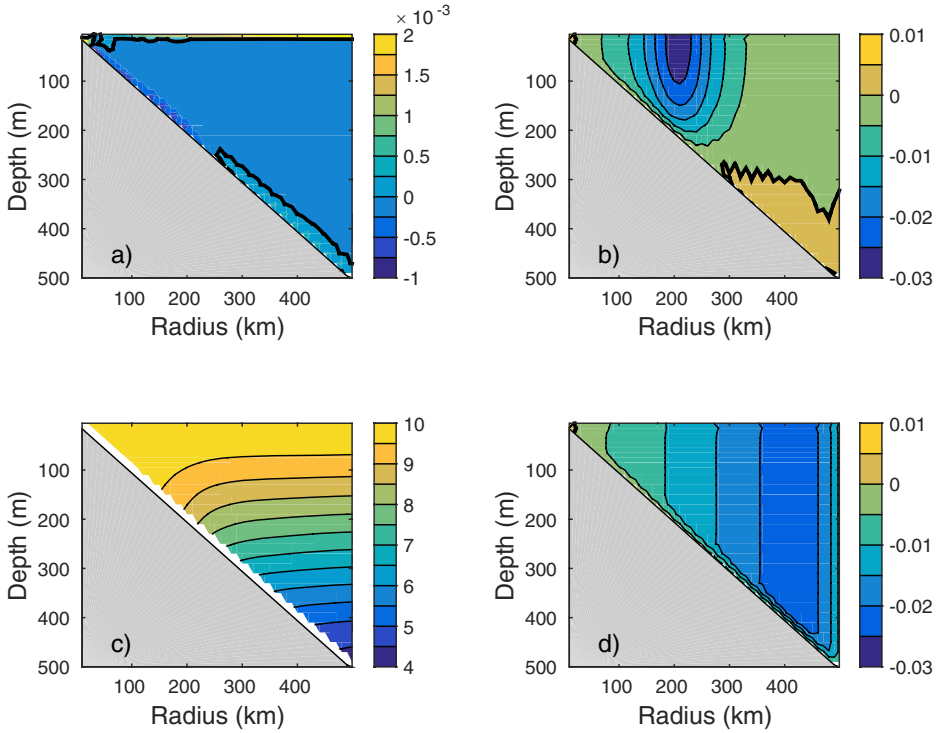
Figure 2. Azimuthally averaged (a) radial velocity (m s^{-1}), (b) azimuthal velocity (m s^{-1}), (c) temperature (°C), and (d) azimuthal velocity (m s^{-1}) for an unstratified calculation. The bold line is the zero contour for velocity.

larger radii, there is a weak flow toward the shallow water near the bottom. There is a net surface flow toward shallow water because the Ekman transport toward the shoal is larger south of the island than is the Ekman transport away from the shoal north of the island as a result of the f^{-1} dependence of the Ekman transport. This is what gives rise to the net Ekman pumping in the domain. Over shallow topography, the flow toward the shallow water in the upper boundary layer is balanced by a flow toward deep water in the bottom boundary layer. This balance no longer holds over deep water. The parameters that control this transition will be discussed in detail subsequently. The azimuthal velocity is negative (anticyclonic) with a maximum value of approximately 3 cm s^{-1} at a radius of 200 km. The stratification is essentially the same as in the initial state over the deep topography, but the isotherms bend downward in shallow water as the sloping bottom is approached. This is a result of the downward flow in the bottom boundary layer advecting the buoyant water downslope. The GM parameterization opposes this isopycnal steepening and results in the equilibrated slopes shown here. It is this horizontal gradient of density in the bottom boundary layer that gives rise to the vertical shear in the azimuthal velocity.
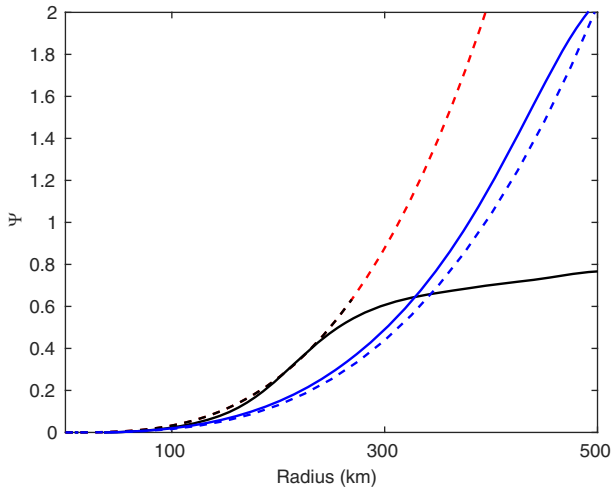
Figure 3. Mean transport as a function of radius for the following: blue dashed line, barotropic theory (equation 8); blue solid line, barotropic model; black dashed line, baroclinic theory (equation 13) for $r < R_m$, and red dashed line for $r > R_m$; and black solid line, baroclinic model.

An otherwise identical calculation was carried out with no stratification. The resulting azimuthal velocity is shown in Figure 2(d). There are several differences compared with the stratified case. The velocity remains anticyclonic and increases in strength out to near the edge of the sloping topography. The velocity is also independent of depth. Finally, the velocity increases more slowly with increasing radius than for the case with stratification.

The average transport streamfunction as a function of radius is shown in Figure 3 for both of these calculations. The transport for the unstratified case (solid blue line) compares well with the theory (equation 8) (dashed blue line). However, the model transport for the stratified case increases more rapidly than for the unstratified case at small radii and then increases only very slowly beyond approximately 250 km radius (solid black line), consistent with the velocity in Figure 2(b). The barotropic theory will now be reconsidered to explain these two major differences, the radial extent of the recirculation and the magnitude of the transport in shallow water.

b. Influences of stratification

It is well known that stratification acts to limit the vertical penetration of vertical velocity in the ocean. Young and Rhines (1982) estimated the depth of penetration of a wind-driven flow assuming that the flow follows a linear vorticity balance ($\beta v = f_0 w_z$) and that the change in planetary vorticity with changing latitude is balanced by stretching [$\beta y = (f_0/N)^2 \psi_{zz}$]. Combining these two constraints, they derived the vertical scale D of the wind-driven flow to be

$$D = \frac{f_0 w^{1/3}}{(\beta N)^{2/3}}.$$ (9)

Utilizing equation (2) for w, the vertical extent of the flow driven by Ekman pumping is

$$D = \left[\frac{\tau_0 f_0}{\rho_0 \beta N^2} \right]^{1/3} = \alpha R_m,$$ (10)

where R_m is the maximum radius at which the flow feels the bottom topography. It is interesting to note that the depth (and radius) of the wind forcing depends on the strength of the wind, it is not an inherent scale of the ocean. For the present calculation, $R_m = 269$ km, in general agreement with the extent of the transport in the baroclinic model in Figure 3 (see also the red line in Fig. 1). This explains why the transport in the stratified case does not increase much beyond this radius despite the fact that the topographic contours are closed.

The other major discrepancy between the stratified case and the theory is that there is a vertical shear in the velocity resulting from the bottom boundary layer. This is the reason why the transport in the baroclinic case increases more rapidly than that predicted by the barotropic theory. This effect can be incorporated into the theory by assuming that the downslope advection of density by the Ekman transport is balanced by an upslope transport driven by the GM parameterization of eddy fluxes. This can be written as

$$C_d U_b = \kappa f_0 s = \frac{\kappa f_0^2 U_z}{N^2},$$ (11)

where U_b is the azimuthal velocity at the bottom, κ is the GM diffusion coefficient, and the subscript z indicates partial differentiation. The final expression on the right-hand side assumes that the vertical shear of the azimuthal velocity is in geostrophic balance with the isopycnal slope s. It is assumed that the azimuthal velocity throughout the water column is the sum of the velocity at the bottom, U_b, and the change in velocity over the bottom boundary layer depth, $U_z \delta$. Solving for U_z from equation (11), the azimuthal velocity is

$$U = U_b \left(1 + \frac{C_d N^2 \delta}{\kappa f_0^2} \right) = \frac{\tau_0 \beta r}{2 \rho_0 f_0 C_d} \left(1 + \frac{C_d N^2 \delta}{\kappa f_0^2} \right),$$ (12)

where it has been assumed for simplicity that $H \gg \delta$.

The transport streamfunction for the stratified case (subscript BC), including the effects of the bottom boundary layer, is then

$$\Psi_{BC} = \int_0^r U H \, dr = \frac{\tau_0 \alpha \beta r^3}{6 \rho_0 f_0 C_d} \left(1 + \frac{C_d N^2 \delta}{\kappa f_0^2} \right).$$ (13)

This prediction is shown on Figure 3 by the dashed black line. This compares very well with the model result out to the radius R_m. Beyond that radius, the theory predicts that the Ekman pumping no longer penetrates to the bottom so that the Sverdrup transport simply flows to
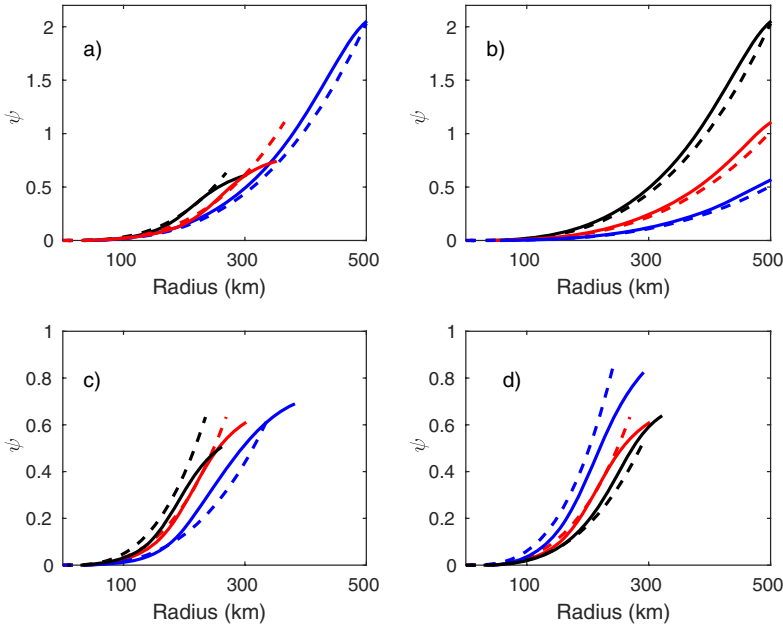
Figure 4. Mean transport as a function of radius for variations in (a) stratification (runs 1, 4, 7), (b) β (barotropic, runs 4, 5, 6), (c) β (baroclinic, runs 1, 2, 3), and (d) Coriolis parameter (runs 1, 12, 13). Solid lines are the model (plotted to $0.8\Psi_{max}$), dashed lines are the theory (equation 8 or 13), plotted to R_m. Blue, red, black indicate increasing value of the relevant parameter.

the south over the topography. As a result, there is no further increase in the recirculation around the topography, in general agreement with the numerical results.

The maximum transport can be calculated for $r = R_m$ to be

$$\Psi_m = \frac{1}{6\alpha^2 C_d} \left(\frac{\tau_0}{\rho_0 N} \right)^2 \left(1 + \frac{C_d N^2 \delta}{\kappa f_0^2} \right). \tag{14}$$

c. Parameter sensitivities

The inclusion of the bottom boundary layer and consideration of the influence of stratification on the vertical scale over which Ekman pumping is felt provides for a simple theoretical prediction of the transport as a function of radius for stratified flows. A series of model calculations with steady forcing have been carried out to test equations (10) and (13), as summarized in Table 1. The azimuthally averaged streamfunction as a function of radius is shown in Figure 4(a) for three values of N^2. The solid lines are diagnosed from the numerical model, and the dashed lines are from equation (13). For clarity, the model curves for those cases with stratification are plotted only out to the radius at which

$\Psi = 0.8\Psi_{max}$, where Ψ_{max} is the maximum transport. The theory is plotted only out to R_m. The model and theory agree well, both in terms of the magnitude of the transport and the radius at which the transport ceases to increase, confirming the scaling (equation 10) and the balance (equation 5). It is interesting to note that although the transport over shallow water decreases with decreasing stratification, because the wind-driven flow penetrates deeper into the water column at low stratification the maximum strength of the recirculation increases with decreasing stratification, as predicted from equation (14).

Variations in β, for cases with no stratification, show a systematic decrease in the transport with decreasing β (Fig. 4b). This is as expected because the forcing (Ekman pumping) is linearly related to β (equation 2). In all cases, the transport increases all the way to the edge of the topography. Transport sensitivity to changes in β for $N^2 = 2.5 \times 10^{-5}$ s^{-2} shows a similar ordering such that the rate of increase in transport decreases with decreasing β, but the radius over which the bottom topography is felt increases (Fig. 4c). The rate of decrease goes as $\beta^{1/3}$, whereas the rate of increase because of deeper penetration goes as $\beta^{-1/3}$ so that the total transport is independent of β, also consistent with equation (14). This is surprising as it is soley because of β that the uniform wind stress drives an Ekman pumping. This result of the transport being independent of β will cease once R_m exceeds the topographic radius.

The final sensitivity shown in Figure 4(d) is because of changes in the Coriolis parameter. Decreasing f_0 decreases the depth of influence, which causes a decrease in the transport, but it increases the velocity as f_0^{-1}. These offset so, absent the bottom boundary layer, the barotropic transport would be insensitive to changes in f_0. However, thermal wind shear in the bottom boundary layer goes as f_0^{-1}, resulting in an increase in transport for decreasing f_0. These trends are well represented in the numerical model.

The radius at which the transport is 80% of its maximum transport has been diagnosed from each of the model runs[3] in Table 1 and plotted against R_m from equation (10) in Figure 5(a). There is generally good agreement for each of the sets of parameter variations. The radius of wind influence is smallest for steep topography, high stratification, weak winds, and small Coriolis parameter.

The shear factor resulting from the bottom boundary layer, $(C_d N^2 \delta)/(\kappa f_0^2)$, is plotted as a function of the model Ψ_{max} in Figure 5(b). The thickness of the bottom boundary layer δ is taken to be the model layer thickness of 20 m because essentially all of the Ekman transport is contained within the deepest model level. Except for the unstratified cases (circles), the shear term increases the transport by between 25% and 200%. This shear term is most important for small κ (square), small f_0 (cross), and large N^2 (triangle).

A comparison between the maximum predicted transport without the bottom boundary layer shear term and that diagnosed from the series of 18 model runs is shown in Figure 5(c). Although some of the model results agree well with the theory, the theory underpredicts the transport for all cases with stratification. There is a set of calculations for which the theory, absent the shear term, predicts 0.32 Sv and the model produces a range between 0.5 Sv

---

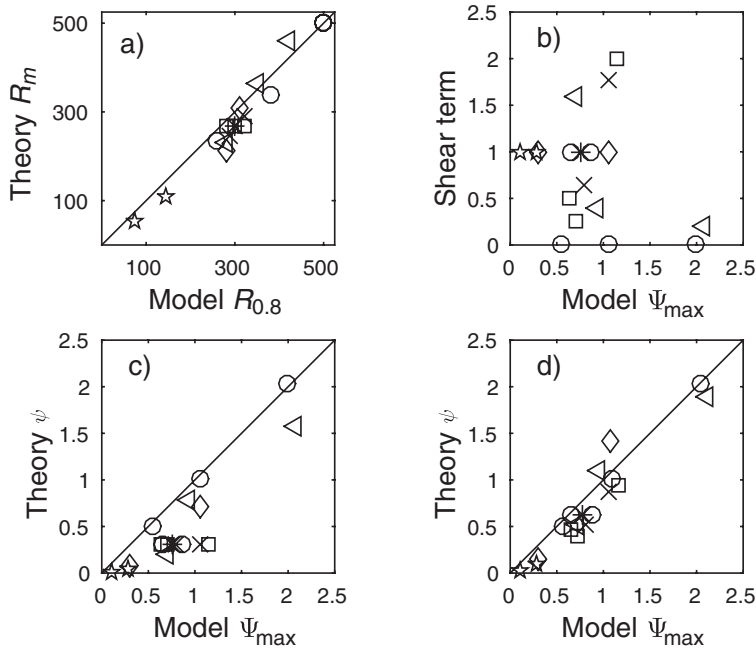3. The unstratified cases are plotted at the radius of maximum transport.

Figure 5. Comparison between model and theory for the series of calculations in Table 1. (a) Radius at which Ψ is 80% maximum in the model compared with R_m from equation (10). (b) Shear term. (c) Maximum model transport versus barotropic theory (equation 8). (d) Maximum model transport versus baroclinic theory (equation 14).

and 1.2 Sv. Including the shear term, as in equation (14), greatly improves the comparison (Fig. 5d). The root-mean-square (RMS) variability of the transport over all calculations is 1.1 Sv. The RMS difference between the model and theory without the shear term is 0.42 Sv, so the theory absent the bottom boundary layer does have some predictive skill. However, with the shear term included the RMS variability between model and theory is reduced to 0.19 Sv.

This topographic influence on the wind-driven circulation can affect not only the circulation around the topographic contours but also the circulation far from the island. Strong wind stress curl is often found in the lee of many islands. A linear vorticity balance requires that meridional advection of planetary vorticity balance the vertical stretching induced by the Ekman pumping. For a dipolar pattern of wind stress curl, this results in a pair of recirculating gyres that extend from the forcing region toward the west. Such recirculations are commonly referred to as a beta plumes (Stommel 1982). These basic dynamics have been used to explain the Hawaiian Lee Counter Current (Belmadani et al. 2013), the Azores Current (Jia 2000), and recirculation in the Labrador and Irminger Seas (Spall and Pickart 2003). A dipolar patch of wind stress curl was placed along the western half of an

island, with and without a topographic skirt (Fig. 6). To the west of the island, the wind is zonal with a maximum eastward stress of 0.05 N m^{-2} at $y = 1,000$ km, which linearly decreases in latitude to zero at $y = 500$ km and $y = 1,500$ km, which is the meridional extent of the bottom topography. This gives a region of uniform positive wind stress curl in the region 1,500 km $< x < 2,000$ km and 1,000 km $< y < 1,500$ km. A similar region of uniform negative wind stress curl lies between 1,500 km $< x < 2,000$ km and 500 km $< y < 1,000$ km. The patch represents the wind stress anomaly that is often found in the lee of islands embedded in a westward wind. The large-scale westward wind stress has been removed in order to not conflate the influences of the uniform westward wind (as previously discussed) and the wind stress curl in the vicinity of the island.

The streamfunction after 10 years of integration is shown in Figure 6(b) for the case with a flat bottom of 500 m depth. As expected, the circulation is dominated by a pair of counterrotating gyres, cyclonic to the north and anticyclonic to the south, that extend all the way to the western boundary. There is a strong zonal flow approaching the island from the west. The same wind stress applied over the linearly sloping bottom topography results in two recirculation gyres aligned to the west of the northern and southern flanks of the topography that are separated by a region of nearly quiescent flow. The flow where the topography is less than the scale depth D is also very weak compared with the flat bottom case. This is because the topographic slope dominates the planetary vorticity gradient such that the linear potential vorticity balance is satisfied with very weak flow because of the strong vertical velocity induced at the bottom (Spall 2001). The topographic beta effectively kills the beta plume where the circulation interacts with the bottom. The recirculation around the closed topographic contours is weak because the net Ekman pumping into the closed contours is nearly zero, so there is no role for the bottom Ekman layer to play in closing the mass budget. This results in only very weak flow toward the island from the west. Thus, the consequences of the local shallow-water dynamics reach far into the interior to the west of the topography by reducing the flow in the Rossby wake of the island and shifting the zonal jets to the northern and southern limits of the topography where the flow no longer reaches the bottom.

3. Time dependence

The circulation response to time-dependent forcing is also of interest. The initial response of a stratified ocean to changes in the wind stress is an excitation of the barotropic mode through changes in the gradient of the sea surface height. The flow perturbation remains barotropic until baroclinic waves can alter the isopycnal slope in the interior of the water column (Anderson and Killworth 1977). These waves communicate information about boundary conditions or inhomogeneity of the wind or topography along the characteristics of the system, typically from east to west for linear, stratified flow over a flat bottom. The flow arrives at its steady state asymptotically as higher and higher baroclinic modes pass by. It is this initial barotropic response that gives the expectation that potentially large recirculations
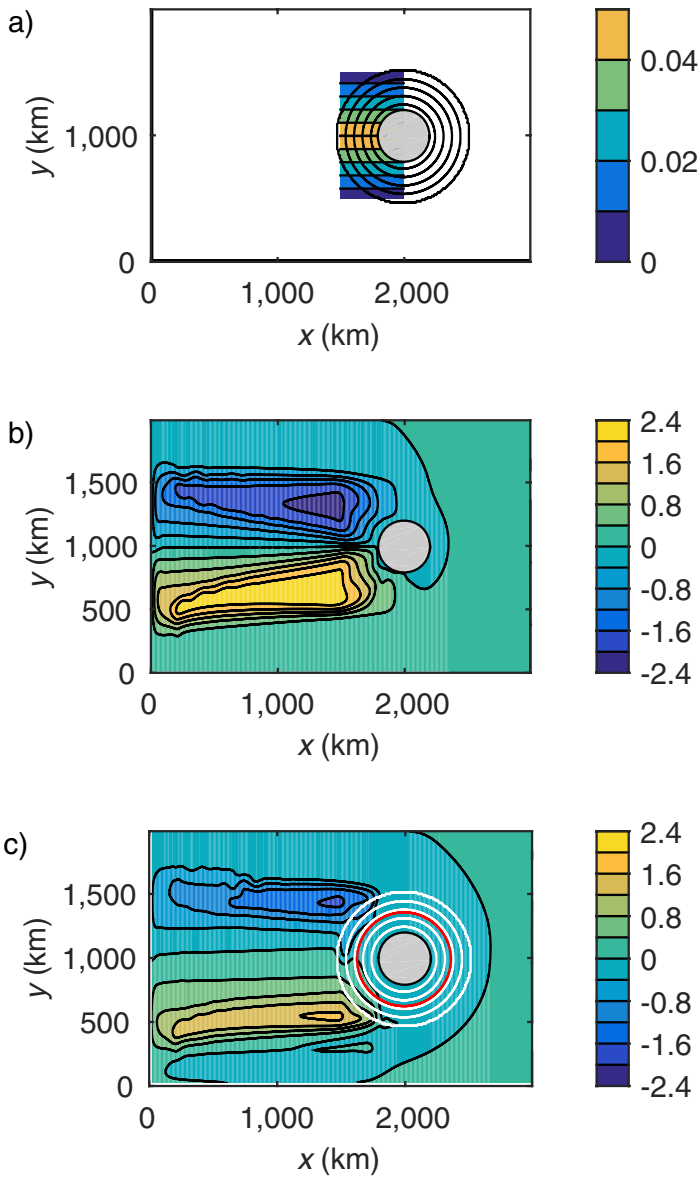
Figure 6. (a) Zonal wind stress (colors) and bottom topography (contours, contour interval 100 m). Transport streamfunction after 10 years for (b) flat bottom, (c) sloping topography shown in panel (a) (contour interval 0.4 Sv).
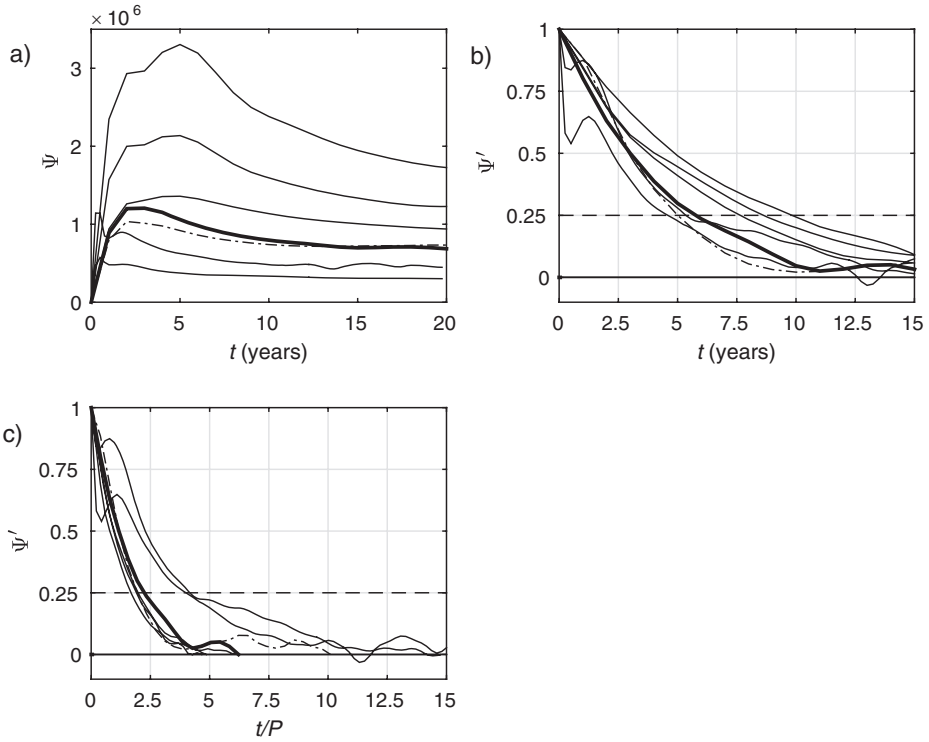
Figure 7. (a) Strength of the topographic recirculation gyre (in Sv) as a function of time. (b) Perturbation transport streamfunction as a function of time. (c) Perturbation transport streamfunction as a function of nondimensional time, scaled by the time it takes a baroclinic Rossby wave to propate the diameter of the topography. The bold line is the central case (run 1 in Table 1), and the dot-dashed line is an otherwise identical calculation in a domain 4,000 km by 3,000 km.

could be driven by time-dependent winds and closed topographic contours, at least for a time, even in the presence of strong stratification.

The strength of the topographic recirculation gyre is plotted as a function of time in Figure 7(a) for seven calculations that were started from rest. The central calculation is given by the bold line; the other lines are for model runs with faster and slower baroclinic Rossby wave speeds or different-sized islands and domains. The general pattern is the same for each run. The recirculation spins up to a maximum recirculation strength and then slowly decays to its steady value. The magnitude of the steady circulation varies between calculations, as expected from the theory in the preceeding section. However, the time to reach the steady solution also varies. In order to better compare the spin-up times, the deviation of ψ from its steady value, normalized by the maximum deviation, is plotted as a function of time relative to the time of the maximum transport (Fig. 7b). Simply stated, the nondimensional perturbation streamfunction Ψ' decays from 1 at time 0 toward 0 over the

decay timescale. The decay rate varies between the calculations such that it takes between approximately 4 years and 10 years for $\psi' = 0.25$.

Based on the results of Anderson and Killworth (1977) for the spin-up of a wind-driven basin, we expect the adjustment to be achieved by the propagation of baroclinic Rossby waves. There are two possible length scales that, together with the baroclinic wave speed, potentially determine the adjustment time: the domain size and the scale of the topography. The case with a zonally elongated domain (dot-dashed line), so that the eastern boundary is 3,000 km to the east of the center of the topography, reaches equilibrium at about the same time, and at the same value, as the central case in which the eastern boundary is 1,000 km from the topography. Thus, the spin-up does not appear to be achieved by information propagating from the eastern boundary of the domain. The other length scale inherent to the problem is the zonal extent of the topography. The time it takes for a baroclinic Rossby wave to propagate across the island is given by

$$P = \frac{2 f_0^2}{\beta \alpha N^2 H}.$$
(15)

The perturbation streamfunction is plotted as a function of time nondimensionalized by P in Figure 7(c). The decay rates now nearly collapse onto a single curve, with $\psi' = 0.25$ for five of the seven runs clustered around $t/P = 2$. Two calculations show a slightly longer decay scale of $t/P \approx 4$, but both of these have a weaker secondary maximum in the recirculation strength early in the calculation. It is not clear why this occurs, but it appears to delay the decay toward the steady solution. The decrease in the transport around the topography reflects a decrease in the circulation at $r > R_m$, where the steady theory predicts weak flow. So the initial response to variations in the wind is for a barotropic circulation to develop over all closed f/h contours. Over the timescale it takes a baroclinic wave to propagate across the topography, the outer barotropic circulation decays, leaving only the inner circulation in the region where the bottom topography remains important. Based on this analysis, it is anticipated that significant barotropic recirculations over the deep topography can be forced by time-dependent winds for timescales less than approximately $2P$.

For a periodic forcing as $\tau = \tau_0(1 + \tau' \sin \omega t)$, where τ' is nondimensional, the barotropic transport streamfunction can be calculated from equation (5) to be

$$\Psi(t) = \int_0^r U H \, dr = \frac{\tau_0 \alpha \beta r^3}{6 \rho_0 f_0 C_d} \left[1 + \frac{\tau' \sin(\omega t + \phi)}{(1 + (\omega H/C_d)^2)^{1/2}} \right],$$
(16)

with

$$\phi = \tan^{-1} \left(\frac{-\omega H}{C_d} \right).$$
(17)

This solution is the same as equation (8) with a sinusoidal term scaled by a factor that depends on the amplitude and frequency of forcing. At frequencies much less than C_d/H, the transport will be in phase with the wind forcing at a magnitude close to its steady value
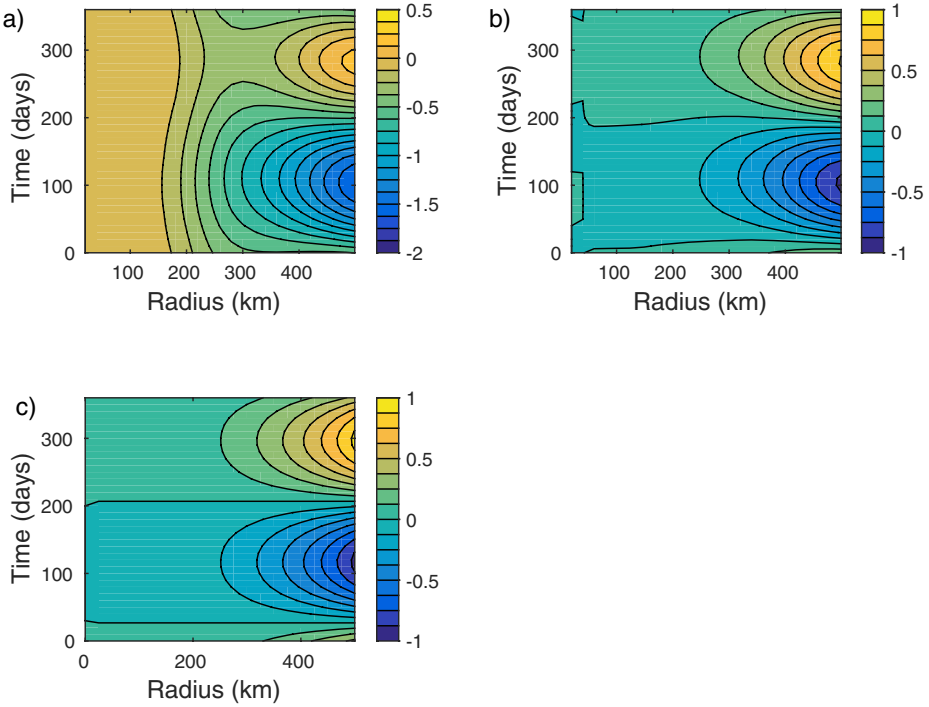
Figure 8. Transport streamfunction as a function of radius and time for the following: (a) full field, (b) mean subtracted at each radius, and (c) theory (equation 16 with mean subtracted at each radius).

for that strength wind. However, for higher frequency forcing the amplitude of the transport variability decreases and the phase of the maximum transport lags the phase of the maximum wind stress. For the central calculation given previously, the transitional frequency at the maximum radius of the topography is $C_d/H = 4 \times 10^{-7} \text{s}^{-1}$ or a forcing period of 0.5 years. This suggests that seasonal variations in the wind stress, where there is a lot of energy, might force significant recirculations over topographic features in the ocean.

The calculation discussed in detail in the preceeding section (run 1) was extended for a period of 720 days with time-dependent forcing of $\tau = \tau_0(1 + 0.5 \sin \omega t)$, where $\omega = 2 \times 10^{-7} \text{ s}^{-1}$ (a forcing period of 360 days). The depth-integrated transport streamfunction as a function of radius and time over the final period of forcing is shown in Figure 8(a). The transport at small radii shows only weak variation in time, but the flow over deep topography is dominated by variability at the forcing frequency. The net transport at radius 500 km changes sign even though the wind stress is always westward and there is always a net downward Ekman pumping. The signal because of the time-dependent forcing is more clearly indicated by subtracting the time-mean at each radius (Fig. 8b). The variability is strongest in deep water with a magnitude exceeding 0.7 Sv. The time-dependent part of the
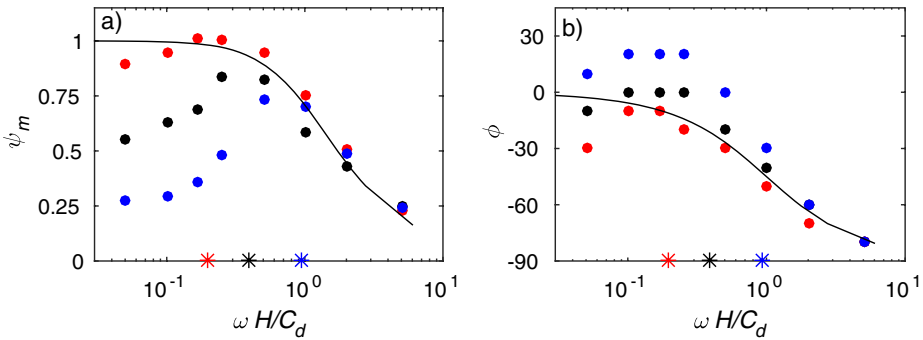
Figure 9. Time-dependent (a) amplitude and (b) phase for a series of model runs (circles) and the theory (black lines) as a function of forcing frequency. Blue, long Rossby wave phase speed $c = 0.03$ m s^{-1}; black, $c = 0.0125$ m s^{-1}; and red, $c = 0.00625$ m s^{-1}. Asterisks indicate frequency for which a baroclinic Rossby wave would propagate a distance equal to the radius of the topography.

theoretical prediction (equation 16) is shown in Figure 8(c). The radial structure, magnitude, and phase all agree reasonably well with that diagnosed from the model.

The model was run with the same initial conditions but with forcing periods that varied between 36 days and 10 years. The amplitude and phase of the azimuthally averaged variability at $r = 500$ km was diagnosed for each of the model runs and is plotted against the theory (equations 16 and 17) in Figure 9 (black circles). The amplitude of the oscillation has been scaled by $(\tau_0 \tau' \alpha \beta r^3)/(6\rho_0 f_0 C_d)$, so the maximum value is 1. The model and theory agree reasonably well at high frequencies, but the model amplitude is significantly lower than that predicted by the theory at low frequencies. The model and theory begin to disagree at a forcing period of 2 years ($\omega H/C_d = 0.25$). The phase found in the model also agrees well with the theory, especially so for the higher frequency cases.

Two other sets of calculations were carried out at the same forcing frequencies but with different values for the first mode baroclinic wave speed through changes in β and N^2. For the standard case, the baroclinic wave speed $c = \beta(NH/f_0)^2 = 0.0125$ m s^{-1}. Calculations with a slower wave speed of 0.00625 m s^{-1} ($\beta = 10^{-11}$ m^{-1} s^{-1}) are indicated by the red circles. The amplitude and frequency are very close to the standard calculations (and theory) at high frequencies but now agree more closely with the theory at low frequencies as well. There is beginning to be a drop-off in amplitude at the lowest frequencies tested. A third set of calculations with $c = 0.03$ m s^{-1} ($\beta = 3 \times 10^{-11}$ m^{-1} s^{-1}, $N^2 = 4 \times 10^{-5}$ s^{-2}) shows a larger decrease in amplitude with decreasing frequency, starting at frequencies less than 0.5 years. This transition from an amplitude that matches the theory for high-frequency forcing to a smaller amplitude at low-frequency forcing occurs roughly at frequency $2\pi c/R$, where R is the maximum radius of the topography and R/c is the time it takes a baroclinic Rossby wave to propagate the radius of the topography. This frequency is marked in Figure 9 by the colored asterisks along the abscissa. This is consistent with the baroclinic adjustment

process in which the initial barotropic response is unbalanced and the transition to the steady circulation is achieved by baroclinic wave propagation. Thus, it is expected that strong time-dependent recirculations can be forced over large topographic features, particularly in regions of slow baroclinic wave speeds.

4. Summary

The primary objective of this study is to better understand the space and time scales over which wind forcing can drive recirculations over regions of closed topographic contours. For unstratified flows, the dynamics reduce to the well-known balance between Ekman transport in the surface boundary layer into the region being balanced by Ekman transport in the bottom boundary layer out of the region (or vice versa). To achieve a net bottom boundary layer transport out of a closed topographic contour requires a recirculation along the contour. The addition of stratification introduces two changes. First, the depth to which the surface Ekman pumping can penetrate is limited (equation 9), consistent with the scaling of Young and Rhines (1982). This will generally reduce the strength of the recirculation. Second, the downslope flow in the bottom boundary layer distorts the isopycnals near the bottom, introducing sloping isopycnals that support a vertical shear in the velocity along the topography. This can result in an increase in the strength of the recirculation by more than a factor of 2.

Time-dependent solutions take the form of a forced damped harmonic oscillator. There are two inherent frequencies in the problem. The first is given by the frictional timescale, which is the bottom depth divided by the linear bottom drag coefficient. For forcing at frequencies less than this the flow approaches a quasi steady state in balance with the forcing. At higher frequencies, the amplitude of the circulation is reduced and the phase lags that of the forcing. The second frequency in the problem is given by the time it takes for a baroclinic Rossby wave to propagate across the region of closed topographic contours. For forcing frequencies higher than this, the circulation is primarily barotropic and the amplitude and phase are well predicted by the barotropic time-dependent theory. However, at lower frequencies the amplitude of the circulation is reduced compared with that predicted by the theory. This is because the circulation at depths greater than the vertical penetration scale D has begun to spin down by Rossby wave radiation. The combination of these two timescales results in an optimal forcing frequency that provides the largest amplitude response.

The approach taken here is very idealized and designed to expose the underlying space and time scales that govern the time-dependent response to wind forcing over regions of closed geostrophic contours provided by bottom topography. The vertical penetration of the wind forcing can result in strong recirculations if there is a net Ekman pumping into the region of closed contours, or it can shut down beta-plume recirculations that would result over a flat bottom if there is no net Ekman pumping. This latter effect will influence the circulation far to the west of the forcing region, so this is more than a local topographic effect. It is expected that strong mean recirculations might be forced around islands, where

there is often large wind stress curl and closed f/h contours. Seasonal variations in wind stress may also force strong recirculations over large-scale topographic features in both the coastal and deep ocean, especially in regions with slow baroclinic wave speeds.

REFERENCES

Anderson, D. L. T., and P. D. Killworth. 1977. Spin-up of a stratified ocean with topography. Deep Sea Res., *24*, 709–732. doi: 10.1016/0146-6291(77)90495-7

Belmadani, A., N. A. Maximenko, J. P. McCreary, R. Furue, O. V. Melnichenko, N. Schneider, and E. Di. Lorenzo. 2013. Linear wind-forced beta plumes with application to the Hawaiian Lee Countercurrent. J. Phys. Oceanogr., *43*, 2071–2094. doi: 10.1175/JPO-D-12-0194.1

de Szoeke, R. A. 1985. Wind-driven mid-ocean baroclinic gyres over topography: A circulation equation extending the Sverdrup relation. J. Mar. Res., *43*, 793–824. doi: 10.1357/002224085788453958

Dewar, W. K. 1998. Topography and barotropic transport control by bottom friction. J. Mar. Res., *56*, 295–328. doi: 10.1357/002224098321822320

Gent, P. R., and J. C. McWilliams. 1990. Isopycnal mixing in ocean circulation models. J. Phys. Oceanogr., *20*, 150–155. doi: 10.1175/1520-0485(1990)020<0150:IMIOCM>2.0.CO;2

Ghaffari, P., P. E. Isachsen, and J. H. LaCasce. 2013. Topographic effects on current variability in the Caspian Sea. J. Geophys. Res.: Oceans, *118*, 7107–7116. doi: 10.1002/2013JC009128

Isachsen, P. E., J. H. LaCasce, C. Mauritzen, and S. Häkkinen. 2003. Wind-driven variability of the large-scale recirculating flow in the Nordic Seas and Arctic Ocean. J. Phys. Oceanogr., *33*, 2534–2550. doi: 10.1175/1520-0485(2003)033<2534:WVOTLR>2.0.CO;2

Jia, Y. 2000. Formation of an Azores Current due to Mediterranean overflow in a mod eling study of the North Atlantic. J. Phys. Oceanogr., *30*, 2342–2358. doi: 10.1175/1520-0485(2000)030<2342:FOAACD>2.0.CO;2

Kamenkovich, V. M. 1962. On the theory of the Antarctic Circumpolar Current. Tr. Inst. Okeanol., *56*, 245–306.

Marshall, J., C. Hill, L. Perelman, and A. Adcroft. 1997. Hydrostatic, quasi-hydrostatic, and nonhydrostatic ocean modeling. J. Geophys. Res., *102*, 5733–5752. doi: 10.1029/96JC02776

Nøst, O. A., and P. E. Isachsen. 2003. The large-scale time-mean ocean circulation in the Nordic Seas and Arctic Ocean estiamted from simplified dynamics. J. Mar. Res., *61*, 175–210. doi: 10.1357/002224003322005069

Spall, M. A. 2001. Large-scale circulations forced by localized mixing over a sloping bottom. J. Phys. Oceanogr., *31*, 2369–2384. doi: 10.1175/1520-0485(2001)031<2369:LSCFBL>2.0.CO;2

Spall, M. A., and R. S. Pickart. 2003. Wind-driven recirculations and exchange in the Labrador and Irminger Seas. J. Phys. Oceanogr., *33*, 1829–1845. doi: 10.1175/2384.1

Stommel, H. 1982. Is the South Pacific helium-3 plume dynamically active? Earth Planet. Sci. Lett., *61*, 63–67. doi: 10.1016/0012-821X(82)90038-3

Sverdrup, H. U. 1947. Wind-driven currents in a baroclinic ocean; with application to the equato rial currents of the eastern Pacific. Proc. Natl. Acad. Sci. U. S. A., *33*, 318–326.

Welander, P. 1968. Wind-driven circulation in one- and two-layer oceans of variable depth. Tellus, *20*, 1–16. doi: 10.1111/j.2153-3490.1968.tb00347.x

Young, W. R., and P. B. Rhines. 1982. A theory of the wind-driven circulation II. Gyres with western boundary layers. J. Mar. Res., *40*, 849–872.